AIAA 2003-1212

Off-Design Performance of a Multi-Stage Supersonic Turbine

Daniel J. Dorney, Lisa W. Griffin
NASA Marshall Space Flight Center
MSFC, AL

Frank W. Huber
Riverbend Design Services
Palm Beach Gardens, FL

Douglas L. Sondak
Boston University
Boston, MA

41th Aerospace Sciences Meeting & Exhibit
6-9 January 2003 / Reno, NV

Off-Design Performance of a Multi-Stage Supersonic Turbine

Daniel J. Dorney*, Lisa W. Griffin§
NASA Marshall Space Flight Center
Applied Fluid Dynamics Analysis Group
MSFC, AL 35812

Frank Huber*
Riverbend Design Services
Palm Beach Gardens, FL 33418

Douglas L. Sondak#
Boston University
Office of Information Technology
Boston, MA 02215

ABSTRACT

The drive towards high-work turbines has led to designs which can be compact, transonic, supersonic, counter rotating, or use a dense drive gas. These aggressive designs can lead to strong unsteady secondary flows and flow separation. The amplitude and extent of these unsteady flow phenomena can be amplified at off-design operating conditions. Pre-test off-design predictions have been performed for a new two-stage supersonic turbine design that is currently being tested in air. The simulations were performed using a three-dimensional unsteady Navier-Stokes analysis, and the predicted results have been compared with solutions from a validated meanline analysis.

NOMENCLATURE

Co	- spouting velocity (ft/sec)
Fr	- radial force (lbf)
Ft	- tangential (circumferential) force (lbf)
Fx	- axial force (lbf)
m	- mass flow (lbm/sec)
M(abs)	- absolute Mach number
M(rel)	- relative Mach number
P	- static pressure (psia)
Power	- Aerodynamic horsepower (HP)
PR	- turbine pressure ratio (total-to-static)
Pt(abs)	- absolute total pressure (psia)
Pt(rel)	- relative total pressure (psia)
R	- reaction based on pressure
Tt(abs)	- absolute total temperature (R)
Tt(rel)	- relative total temperature (R)
U	- Pitchline rotor velocity (ft/sec)
U/Co	- Isentropic velocity ratio
W	- work based on mass-avg (BTU/lbm)
α	- absolute circumferential flow angle, (deg)
β	- relative circumferential flow angle, (deg)
η(ts)	- stage total-to-static efficiency
η(tt)	- stage total-to-total efficiency
η(ots)	- overall turbine total-to-static efficiency

* Aerospace Engineer, Associate Fellow AIAA.
§ Team Leader, Senior Member AIAA.
* President, Senior Member AIAA.
# Senior Scientific Programmer, Senior Member AIAA.

η(ott) - overall turbine total-to-total efficiency
ω - RPM

INTRODUCTION

Modern high-work turbines can be compact, transonic, supersonic, counter-rotating, and can use a dense drive gas. The vast majority of modern rocket turbine designs fall into these categories. These turbines are often characterized by large amounts of flow unsteadiness. The flow unsteadiness can have a major impact on turbine performance and durability. For example, the Space Transportation Main Engine (STME) fuel turbine, a high-work transonic design was found to have an unsteady inter-row shock that reduced efficiency by 2 points and increased dynamic loading by 24 percent. The Revolutionary Reusable Technology Turbopump (RRTT), which uses full flow oxygen for its drive gas, was found to shed vortices with such energy as to raise serious blade durability concerns. In both cases, the sources of the problems were uncovered before turbopump testing with the application of validated unsteady computational fluid dynamics (CFD) to the designs. In the case of the RRTT and the Alternate Turbopump Development (ATD) turbines, the unsteady CFD codes were used not just to identify problems, but also to guide designs that mitigate problems due to unsteadiness. The incorporation of unsteady flow analyses into the design process has led to turbine designs with higher performance and fewer dynamics problems. References 1-4 are examples of the application of unsteady CFD to rocket turbine designs.

Recently, CFD has been used in the design of a two-stage supersonic turbine that is currently being tested at NASA Marshall Space Flight Center (see Refs. 5 and 6). Meanline, two-dimensional CFD and three-dimensional CFD analyses were used in conjunction with optimization techniques to design both the flow path and the airfoil geometries. The turbine is being tested at both design and off-design operating conditions. As part of the pre-test effort unsteady three-dimensional flow simulations have been performed at several off-design conditions and the results compared with results from a validated meanline analysis. The objective of the current work is to quantify the performance of the turbine at off-design flow conditions, as well as to characterize changes in the unsteadiness as a function of flow condition.

NUMERICAL PROCEDURES

The meanline code uses a combination of the one-dimensional equations of motion and empirical loss models to predict the flow and performance quantities in the turbine. The meanline analysis used in this study has been anchored on many experimental data sets (e.g., subsonic, transonic and supersonic), including those shown in Fig. 1.

The governing equations in the CFD analysis are the time-dependent, three-dimensional Reynolds-averaged Navier-Stokes equations. The algorithm consists of a time marching, implicit, finite-difference scheme. The procedure is third-order spatially accurate and second-order temporally accurate. The inviscid fluxes are discretized according to the scheme developed by Roe [7]. The viscous fluxes are calculated using standard central differences. An approximate-factorization technique is used to compute the time rate changes in the primary variables. Newton sub-iterations are used at each global time step to increase stability and reduce linearization errors. For all cases investigated in this study, one Newton sub-iteration was performed at each time step. The turbulent viscosity is calculated using the two-layer Baldwin-Lomax algebraic turbulence model [8]. The code has been parallelized using Message Passing Interface (MPI) and OpenMP application program interfaces (API's) to reduce the computation time for large-scale three-dimensional simulations.

The Navier-Stokes analysis uses O- and H-type zonal grids to discretize the flow field and facilitate relative motion of the rotating components (see Fig. 2). The O-grids are body-fitted to the surfaces of the airfoils and generated using an elliptic equation solution procedure. They are used to properly resolve the viscous flow in the blade passages and to easily apply the algebraic turbulence model. The algebraically generated H-grids are used to discretize the remainder of the flow field.

The CFD analysis has been validated on several supersonic turbine geometries (e.g., Refs. 1-3).

BOUNDARY CONDITIONS

The theory of characteristics is used to determine the boundary conditions at the inlet and exit of the computational domain. For subsonic inlet flow the total pressure, total temperature, and the circumferential and radial flow angles are specified as a function of the radius. The upstream running

Riemann invariant is extrapolated from the interior of the computational domain.

For subsonic outflow the circumferential and radial flow angles, total pressure, and the total temperature are extrapolated from the interior of the computational domain. The total-to-static pressure ratio is specified at mid-span of the computational exit and the pressure at all other radial locations at the exit is obtained by integrating the equation for radial equilibrium. Periodicity is enforced along the outer boundaries of the H-grids in the circumferential direction.

At solid surfaces the relative velocity is set to zero, the normal derivative of the pressure is set to zero, and the surfaces are assumed to be adiabatic.

GEOMETRY AND FLOW CONDITIONS

The two-stage supersonic turbine configuration is typical of those proposed for a reusable launch vehicle. The experimental rig is a 70% scale version of the actual turbine and has 12 first-stage vanes, 30 first-stage rotors, 73 second-stage vanes and 56 second-stage rotors (see Fig. 3). In the current effort, a 15-vane/30-rotor/75-vane/60-rotor airfoil approximation has been made, resulting in a simulation blade count of 1/2/5/4. To keep the pitch-to-chord ratio (blockage) constant, the first-stage vanes were scaled by a factor of 12/15, the second-stage vanes were scaled by a factor of 73/75 and the second-stage rotors were scaled by a factor of 56/60. The tip clearance in the first- and second-stage rotors was set at the design value of approximately 2% of the respective rotor heights.

The total number of grid points used to discretize the turbine was 4,139,957. Figure 2 illustrates an x-y view of the grids at midspan, where every other grid point in each coordinate direction has been removed for clarity. The average value of y+, the non-dimensional distance of the first grid line above the surface was approximately 1.0 for the airfoil surfaces and 1.5 for the endwall surfaces.

The simulations were run on 48 400-MHz R12000 processors of an SGI Origin2000. Each simulation was run for 15 global cycles (which constitutes on complete rotor revolution) at 22,000 time steps per cycle. A global cycle is defined as the time it takes for the two first-stage rotor blades to pass by one first-stage vane airfoil. The value of 22,000 iterations per cycle was chosen to resolve all the expected frequencies of interest. A time step required an average of 8.0 seconds CPU time on each of 48 (24 MPI processes, with 2 OpenMP threads per MPI process) processors. The time periodicity of the solutions was determined by interrogating pressure traces at specific points along the airfoil surfaces.

RESULTS

Simulations have been performed at the design flow conditions, as well as four off-design flow conditions. The pressure ratios and rotational speeds of all five test cases are presented in Fig. 4 and tabulated in Tables 1 to 5. The four off-design flow conditions were chosen to lie on the bounds of the test envelope. Tables 1 to 5 also contain flow and performance quantities from the meanline and Navier-Stokes (CFD) analyses.

Turbine performance curves predicted using the meanline and CFD codes are shown in Figs. 5 and 6. In Figs. 5 and 6 the pressure ratios refer to the total pressure at the inlet to the first-stage vane and the static pressure at the exit of the second-stage rotor. The shapes of the curves are similar, although the meanline code consistently predicts higher efficiencies. The differences in the efficiencies are to be expected because there is little experimental data available for anchoring the meanline and CFD analyses for supersonic turbines at off-design operating conditions. Other observations from comparing the CFD and meanline results in Tables 1 to 5 include:

1) The mass flow rate predicted by the CFD analysis is consistently 5% greater than that predicted by the meanline analysis.
2) The CFD simulations show significantly more underturning of the flow in the first-stage rotor compared to the meanline results. The meanline analysis yields correspondingly more work in the first stage.
3) In general, except for the off-2 flow conditions, the CFD analysis predicts more work being produced by the second stage. The resulting work splits between the first and second stages are different in the two analyses.

One of the goals of the experimental portion of the development program is to provide a detailed data set at off-design operating conditions for anchoring codes.

The remainder of this section will focus on only two of the operating conditions for brevity: the design flow condition and the case with a pressure ratio of approximately 12 (designated as off-3). This off-design condition was chosen because it showed the largest deviations from the design flow conditions.

Figures 7 and 8 display midspan instantaneous absolute Mach contours from the two cases. In both simulations the flow enters the vane passage at a low subsonic Mach number. The flow accelerates through the vane passage, reaching sonic (choked) conditions at the throat. The flow becomes supersonic in the diverging portion of the vane passage, reaching a peak number of approximately 1.8. A strong expansion wave system emanates from the pressure side of the trailing edge. The expansion waves move across the vane passage and interact with the suction surface of the adjacent vane. The vane wakes convect into the rotor passage where they interact with the rotor bow shock. This interaction creates a subsonic flow region near the leading edge that weakens the boundary layer and increases the extent of the rotor suction surface separated flow region. This condition exists until the rotor passes through the vane wake. The flow diffuses as it exits the rotor passage, decelerating back to subsonic flow conditions. The fluctuations in the size of the separated flow region on the suction surface of the rotor result in incidence variations in the flow entering the second-stage vane. The incidence variations induce periodic separation on the pressure surface of the vane. During the turbine design process the axial gap between the two stages was varied to minimize the incidence variations. The flow reaccelerates in the vane passage, reaching sonic conditions near the passage exit. The subsequent shock pattern is stronger at the off-design flow conditions. In both cases the flow remains subsonic in the second-stage rotor, although the exit Mach number is higher at the off-design conditions because of the larger pressure ratio (also see Tables 1 and 4).

Figures 9 and 10 show instantaneous entropy contours at midspan for the two cases. Both figures illustrate the "wagging" of the first-stage vane wake due to the periodic passing of the rotor blades and the interaction with the rotor shock system. The variations in the rotor suction surface separation are highlighted in the rotor passage. The increased separation at the off-design flow conditions causes underturning of the flow, which is also evident by comparing the time-averaged rotor exit flow angles in Tables 1 and 4. Vortex shedding from the trailing edge of the second-stage vane is observed at both flow conditions, although it appears to be stronger at the off-design conditions.

Unsteady pressure envelopes for the two operating conditions are shown in Figs. 11 and 12. The predicted solutions for the first-stage vane are similar at both operating conditions, which is expected since the vane remains choked at both pressure ratios. The only appreciable unsteadiness on the first-stage vane occurs downstream of the throat on the suction surface. The first-stage rotor displays significant unsteadiness over the first 25% of the axial chord on the suction surface. This unsteadiness is generated through a combination of the passing vane wakes, the vane trailing edge expansion fans, and the temporal variations of the rotor bow shock. The amplitude of the unsteadiness in this region is greater at the off-design conditions. The remainder of the rotor surface (at both operating conditions) exhibits a moderate amount of unsteadiness, which is generated by the first-stage vane wakes, interaction with the potential fields of the upstream and downstream vane rows and the intermittent separation of the rotor suction-surface boundary layer. The effects of the suction surface flow separation are evident from approximately X/C=0.80 to the trailing edge. The pressure envelopes on the second-stage vane and rotor are, in general, similar at both flow conditions. The exception is near the along the suction surface of the second-stage rotor. The amplitude of the unsteadiness in this region is slightly greater at the design flow conditions.

Unsteady pressure traces and Fourier decompositions at midspan of the first-stage vane trailing edge, first-stage rotor leading edge and second-stage vane trailing edge are shown in Figs. 13-24. These locations were chosen for presentation because they exhibit the greatest amount of unsteadiness. The pressure variations at the trailing edge of the first-stage vane (see Figs. 13-16) are mainly at the rotor-passing frequency (5206 Hz at the design conditions and 5468 Hz for the off-3 conditions). The distribution at the off-design flow conditions also displays significant unsteadiness at half the rotor passing frequency. This additional frequency may be a result of increased "wagging" of the vane wakes. A large amount of the unsteadiness at the leading edge of the first-stage rotor (see Figs. 17-20) is generated by the periodically passing vane wakes (2608 Hz and 2734 Hz, respectively). The unsteadiness at the wake passing frequency (the large peaks in Figs. 17 and 19) is enhanced by the fact that these wakes periodically eliminate the rotor leading edge bow shock. A significant amount of unsteadiness is also generated at twice the vane wake passing frequency, and is caused by periodic variations in the rotor bow shock system and the interaction of the bow shocks with the adjacent rotors. The frequency spectrum for the rotor leading edge is much richer (in both cases) than that observed at the vane trailing edge. Undoubtedly the periodic fluctuations in the extent of the rotor suction surface separation and variations in the strength of the shock system contribute to these additional frequencies. The pressure traces at the trailing edge of the second-stage (see Figs. 21-24) vane exhibit the

high-frequency unsteadiness associated with vortex shedding. The vortex shedding frequency occurred at approximately 110 kHz (corresponding to a Strouhal number of approximately 0.22). The vortex shedding does not occur continuously, but appears and disappears as a function of the position of the first-stage rotor. This may be a direct consequence of the incidence variations discussed previously.

Radial profiles of the circumferentially and time-averaged absolute Mach number are shown in Figs. 25 and 26. The shapes of the profiles are similar in the first-stage for both operating conditions, which is expected because the first-stage vane is choked in both cases. The Mach number profiles are also similar at the exit of the second-stage vane. The shapes of the profiles at the exit of the second-stage rotor are similar, but the off-design case shows higher quantitative levels because the flow expands to achieve the larger pressure ratio. In both simulations the footprint of the rotor tip clearance flows can be seen outboard of 80% span. In both simulations there is more spanwise distribution of the flow in the first-stage rotor than in any other blade row. This phenomenon is caused by the rotor bow shock system and separated flow region, which vary spatially as well as temporally.

Integrated unsteady forces on the rotors are shown in Figs. 27-30, respectively. The unsteady forces (amplitude and magnitude) on the first-stage rotor are similar at both operating conditions. The variations in the tangential force occur primarily at the passing frequency of the first-stage vanes. The average forces on the second-stage rotor are greater at the off-design condition, which is again consistent with the larger pressure ratio. The force variations in the second stage occur across a wide range of frequencies.

CONCLUSIONS

A series of meanline and unsteady three-dimensional Navier-Stokes simulations have been conducted to provide pre-test performance and unsteadiness predictions for a two-stage supersonic turbine. The performance and flow quantities predicted using the meanline and Navier-Stokes analyses show reasonable agreement over a wide range of flow conditions. Investigation of the unsteady flow field revealed a complex interaction of wakes, expansion fans, shock waves and separated flow regions. The unsteady pressure fields predicted in this study were used to help determine the locations of the transducers in the experiments. The predicted results will be compared to the experimental data during the next several months, and will be presented in a future paper.

ACKNOWLEDGEMENTS

The authors would like to acknowledge the use of the supercomputer facilities at NASA Ames Research Center, and especially thank Mr. Chuck Niggley for his assistance.

REFERENCES

1. Griffin, L. W. and Dorney, D. J., ``Simulations of the Unsteady Flow Through the Fastrac Supersonic Turbine,'' *ASME Journal of Turbomachinery*, Vol. 122, No. 2, April, 2000, pp. 225-233.

2. Dorney, D. J., Griffin, L. W., and Huber, F., ``A Study of the Effects of Tip Clearance in a Supersonic Turbine,'' *ASME Journal of Turbomachinery*, Vol. 122, No. 4, October, 2000, pp. 674-673.

3. Dorney, D. J., Griffin, L. W., Huber, F., and Sondak, D. L., ``Full- and Partial-Admission Performance of the Simplex Turbine,'' AIAA Paper 2002-3638, 38th AIAA/ASME/SAE/ASEE Joint Propulsion Conference, Indianapolis, IN, July 7-10, 2002, also accepted for publication in the *AIAA Journal of Propulsion and Power.*

4. Marcu, B., Tran, K. and Wright, B., ``Prediction of Unsteady Loads and Analysis of Flow Changes Due to Turbine Blade Manufacturing Variations During the Development of Turbines for the MB-XX Upper Stage Engine,'' AIAA Paper 2002-4162, 38th AIAA/ASME/SAE/ASEE Joint Propulsion Conference, Indianapolis, IN, July 7-10, 2002.

5. Griffin, L. W., Dorney, D. J., Huber, F. W., Tran, K., Shyy, W., and Papila, N., ``Detailed Aerodynamic Design Optimization of an RLV Turbine,'' AIAA 2001-3397, 37th AIAA/ASME/SAE/ASEE Joint Propulsion Conference, Salt Lake City, UT, July 8-11, 2001.

6. Dorney, D. J., Griffin, L. W., Huber, F., Sondak, D. L., ``Effects of Endwall Geometry and Stacking on Two-Stage Supersonic Turbine Performance," AIAA 2002-0078, AIAA 2002-0078, 40th AIAA Aerospace Sciences Meeting and Exhibit, Reno, NV, January 14-17, 2002, also AIAA Journal of Propulsion and Power, Vol. 18, No. 6, pp. 1305-1307, Nov-Dec, 2002.

7. Roe, P. L., ``Approximate Riemann Solvers, Parameter Vectors, and Difference Schemes,'' *Journal of Computational Physics*, Vol. 43, 1981, pp. 357-372.

8. Baldwin, B. S., and Lomax, H., ``Thin Layer Approximation and Algebraic Model for Separated Turbulent Flow,'' AIAA Paper 78-257, Huntsville, AL, January, 1978.

Value	Vane-1 Inlet (cfd)	Vane-1 Inlet (meanln)	Rotor-1 Inlet (cfd)	Rotor-1 Inlet (meanln)	Vane-2 Inlet (cfd)	Vane-2 Inlet (meanln)	Rotor-2 Inlet (cfd)	Rotor-2 Inlet (meanln)	Rotor-2 Exit (cfd)	Rotor-2 Exit (meanln)
ω			10413.	10413.			10413.	10413.	10413.	10413.
PR									8.85	8.85
M(abs)	0.079	0.077	1.35	1.53	0.60	0.89	1.08	1.04	0.61	0.57
M(rel)	0.079	0.077	1.05	1.21	0.60	0.89	0.79	0.73	0.85	0.85
P	70.0	69.7	20.4	16.4	18.0	12.6	9.70	9.70	7.98	8.04
Pt(abs)	70.3	70.0	60.6	62.5	23.3	21.0	20.2	19.1	10.3	10.0
Pt(rel)	70.3	70.0	40.7	40.1	23.3	21.0	14.7	13.9	12.8	12.9
Tt(abs)	760.	760.	759.	760.	630.	608.	628.	608.	538.	521.
Tt(rel)	760.	760.	678.	670.	630.	608.	573.	556.	572.	556.
α	0.0	0.0	79.0	79.7	-56.9	-70.0	66.7	69.9	-35.7	-43.4
β	0.0	0.0	75.5	78.3	-56.9	-70.0	56.7	60.1	-54.6	-60.0
m	4.35	4.16	4.38	4.16	4.40	4.16	4.48	4.16	4.50	4.16
Power			179.	215.			138.	124.1		
W			31.4	36.5					22.1	21.1
R			0.040	0.062					0.159	0.353
η(ts)			0.534	0.519					0.553	0.600
η(tt)			0.633	0.687					0.701	0.756
η(ots)									0.632	0.684
η(ott)									0.693	0.740

Table 1. CFD and meanline predictions at design flow conditions

Value	Vane-1 Inlet (cfd)	Vane-1 Inlet (meanln)	Rotor-1 Inlet (cfd)	Rotor-1 Inlet (meanln)	Vane-2 Inlet (cfd)	Vane-2 Inlet (meanln)	Rotor-2 Inlet (cfd)	Rotor-2 Inlet (meanln)	Rotor-2 Exit (cfd)	Rotor-2 Exit (meanln)
ω			12471.	12471.			12471.	12471.	12471.	12471.
PR									8.85	8.85
M(abs)	0.078	0.077	1.32	1.48	0.51	0.71	1.02	0.95	0.55	0.53
M(rel)	0.078	0.077	0.95	1.09	0.51	0.71	0.68	0.59	0.82	0.86
P	70.0	69.7	21.5	17.7	18.8	14.8	10.2	10.8	7.98	7.91
Pt(abs)	70.3	70.0	61.0	63.2	22.7	20.8	19.9	19.2	9.84	9.56
Pt(rel)	70.3	70.0	38.7	37.9	22.7	20.8	14.0	13.7	12.5	12.8
Tt(abs)	760.	760.	759.	760.	617.	594.	616.	594.	522.	500.
Tt(rel)	760.	760.	667	657.	617.	594.	558.	539.	559.	539.
α	0.0	0.0	79.4	80.1	-52.6	-68.4	66.9	68.4	-28.7	-38.3
β	0.0	0.0	74.9	78.0	-52.6	-68.4	53.0	55.9	-54.4	-60.2
m	4.35	4.17	4.30	4.17	4.41	4.17	4.46	4.17	4.51	4.17
Power			198.	235.2			143.	132.8		
W			34.3	39.9					22.9	22.5
R			0.047	0.050					0.198	0.403
η(ts)			0.598	0.613					0.598	0.656
η(tt)			0.679	0.745					0.727	0.795
η(ots)									0.677	0.738
η(ott)									0.729	0.789

Table 2. CFD and meanline predictions at off-1 flow conditions

Value	Vane-1 Inlet (cfd)	Vane-1 Inlet (meanln)	Rotor-1 Inlet (cfd)	Rotor-1 Inlet (meanln)	Vane-2 Inlet (cfd)	Vane-2 Inlet (meanln)	Rotor-2 Inlet (cfd)	Rotor-2 Inlet (meanln)	Rotor-2 Exit (cfd)	Rotor-2 Exit (meanl)
ω			5881.	5881.			5881.	5881.	5881.	5881.
PR									8.85	8.85
M(abs)	0.079	0.077	1.41	1.61	0.86	1.15	1.13	1.58	0.79	0.73
M(rel)	0.079	0.077	1.24	1.42	0.86	1.15	0.97	1.36	0.93	0.90
P	70.0	69.7	18.6	14.5	15.4	10.9	9.49	5.02	7.98	7.91
Pt(abs)	70.3	70.0	60.0	61.3	25.7	24.7	21.3	19.3	12.1	11.3
Pt(rel)	70.3	70.0	47.2	47.0	25.7	24.7	17.5	15.0	14.0	13.4
Tt(abs)	760.	760.	759.	760.	668.	663	667.	663	602.	593.
Tt(rel)	760.	760.	708.	704.	668.	663.	630.	617.	628.	617.
α	0.0	0.0	78.3	79.0	-63.7	-72.2	66.2	61.6	-47.6	-52.5
β	0.0	0.0	76.4	78.9	-63.7	-72.2	61.7	60.3	-55.4	-59.5
m	4.35	4.16	4.37	4.16	4.46	4.16	4.57	4.16	4.60	4.16
Power			123.	138.			88.	99.		
W			22.1	23.4					15.8	16.8
R			0.054	0.055					0.182	-1.07
η(ts)			0.342	0.313					0.347	0.380
η(tt)			0.479	0.498					0.509	0.525
η(ots)									0.448	0.475
η(ott)									0.525	0.542

Table 3. CFD and meanline predictions at off-2 flow conditions

Value	Vane-1 Inlet (cfd)	Vane-1 Inlet (meanln)	Rotor-1 Inlet (cfd)	Rotor-1 Inlet (meanln)	Vane-2 Inlet (cfd)	Vane-2 Inlet (meanln)	Rotor-2 Inlet (cfd)	Rotor-2 Inlet (meanln)	Rotor-2 Exit (cfd)	Rotor-2 Exit (meanln)
ω			10934.	10934.			10934.	10934.	10934.	10934.
PR									11.63	11.63
M(abs)	0.079	0.077	1.32	1.52	0.57	0.84	1.06	1.03	0.79	0.75
M(rel)	0.079	0.077	1.01	1.18	0.57	0.84	0.76	0.71	1.04	1.07
P	70.0	69.7	21.2	16.5	18.4	13.3	9.90	9.81	6.05	6.02
Pt(abs)	70.3	70.0	61.0	62.6	23.4	20.9	20.3	19.1	9.2	8.8
Pt(rel)	70.3	70.0	40.5	39.4	23.4	20.9	14.6	13.7	12.2	12.4
Tt(abs)	760.	760.	759.	760.	627.	604.	626	604.	525.	504.
Tt(rel)	760.	760.	676.	666.	627.	604	570.	550.	569.	550.
α	0.0	0.0	79.3	79.7	-55.7	-69.7	66.8	68.2	-36.3	-45.2
β	0.0	0.0	75.5	78.2	-55.7	-69.7	55.9	59.3	-52.9	-59.2
m	4.35	4.17	4.40	4.17	4.44	4.17	4.50	4.17	4.57	4.17
Power			182.	221.			159.	142.		
W			32.0	37.4					24.7	24.0
R			0.049	0.055					0.303	0.511
η(ts)			0.551	0.545					0.511	0.553
η(tt)			0.646	0.704					0.698	0.753
η(ots)									0.614	0.668
η(ott)									0.702	0.753

Table 4. CFD and meanline predictions at off-3 flow conditions

Value	Vane-1 Inlet (cfd)	Vane-1 Inlet (meanln)	Rotor-1 Inlet (cfd)	Rotor-1 Inlet (meanln)	Vane-2 Inlet (cfd)	Vane-2 Inlet (meanln)	Rotor-2 Inlet (cfd)	Rotor-2 Inlet (meanln)	Rotor-2 Exit (cfd)	Rotor-2 Exit (meanl)
ω			8769.	8769.			8769.	8769.	8769.	8769.
PR									4.00	4.00
M(abs)	0.079	0.077	1.31	1.66	0.56	0.74	0.61	0.61	0.26	0.24
M(rel)	0.079	0.077	1.04	1.37	0.56	0.74	0.40	0.38	0.42	0.44
P	70.0	69.7	21.6	13.1	20.8	17.1	18.4	18.5	17.6	17.5
Pt(abs)	70.3	70.0	61.0	60.4	26.3	24.4	23.9	23.8	18.4	18.2
Pt(rel)	70.3	70.0	43.7	40.5	26.3	24.4	20.6	20.5	19.8	20.0
Tt(abs)	760.	760.	760.	760.	651.	634.	651.	634.	613.	593.
Tt(rel)	760.	760.	691.	678.	651.	634.	625.	607.	626.	607.
α	0.0	0.0	79.4	78.4	-57.8	-71.8	66.2	69.0	-17.0	-31.4
β	0.0	0.0	76.5	77.6	-57.8	-71.8	50.1	56.5	-53.2	-61.1
m	4.25	4.16	4.32	4.16	4.43	4.16	4.50	4.16	4.58	4.16
Power			155.	178.			56.3.	58.2		
W			26.1	30.3					9.2	9.9
R			0.012	-0.080					0.259	-2.60
η(ts)			0.499	0.503					0.547	0.691
η(tt)			0.592	0.646					0.621	0.779
η(ots)									0.603	0.674
η(ott)									0.612	0.691

Table 5. CFD and meanline predictions at off-4 flow conditions

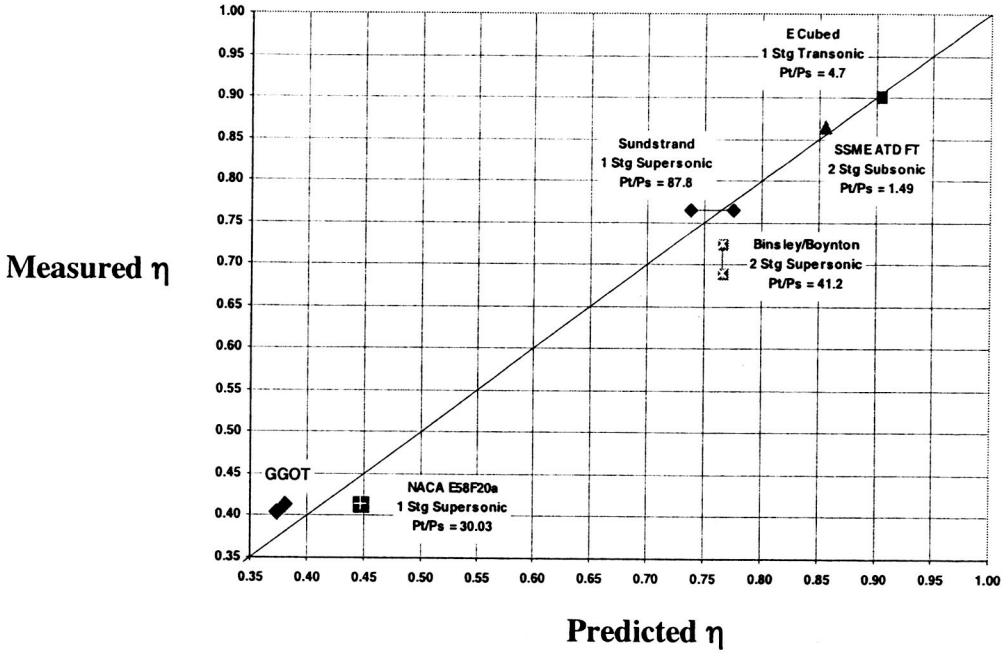

Figure 1. Meanline code validation cases

Figure 2. Turbine midspan computational grid

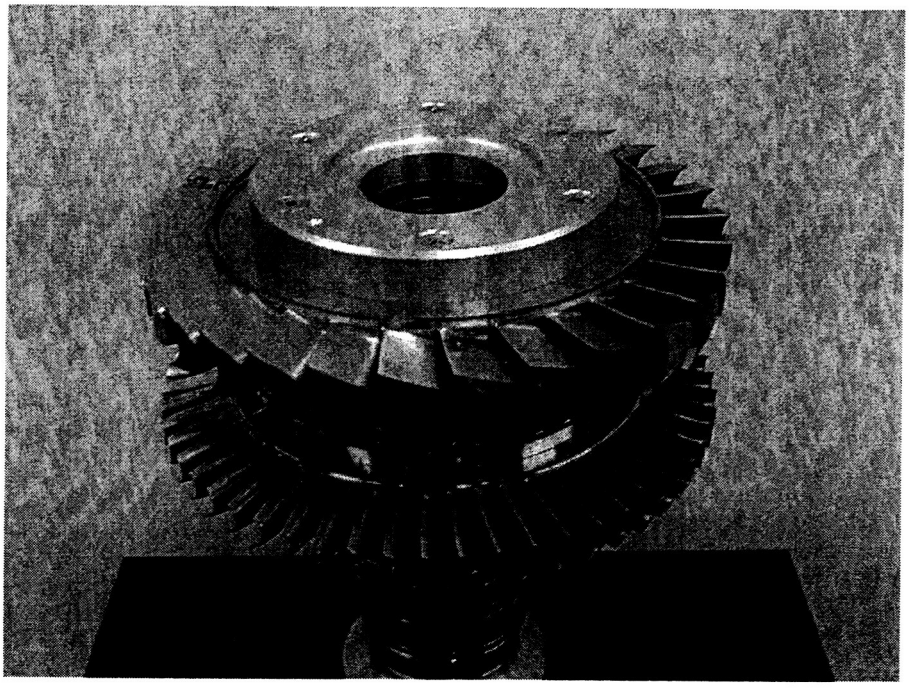

Figure 3. Turbine experimental apparatus (rotors only)

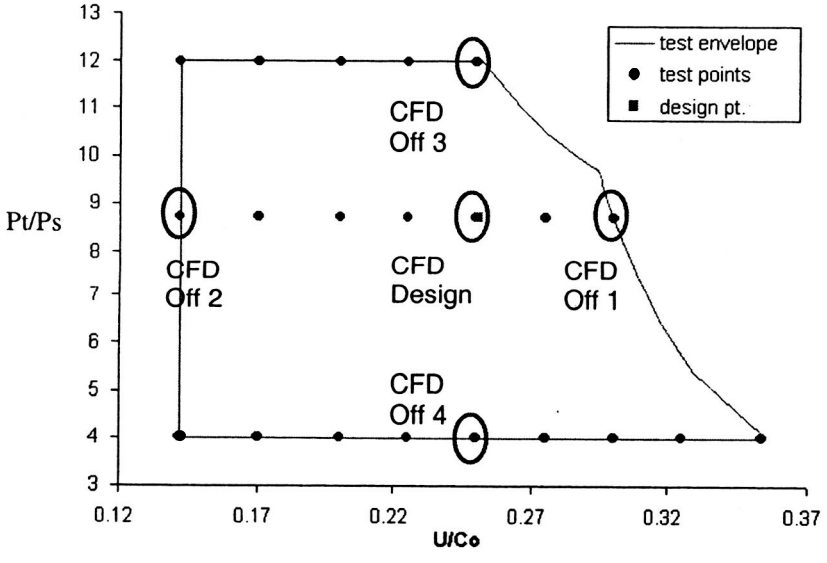

Figure 4. Experimental and CFD test matrix

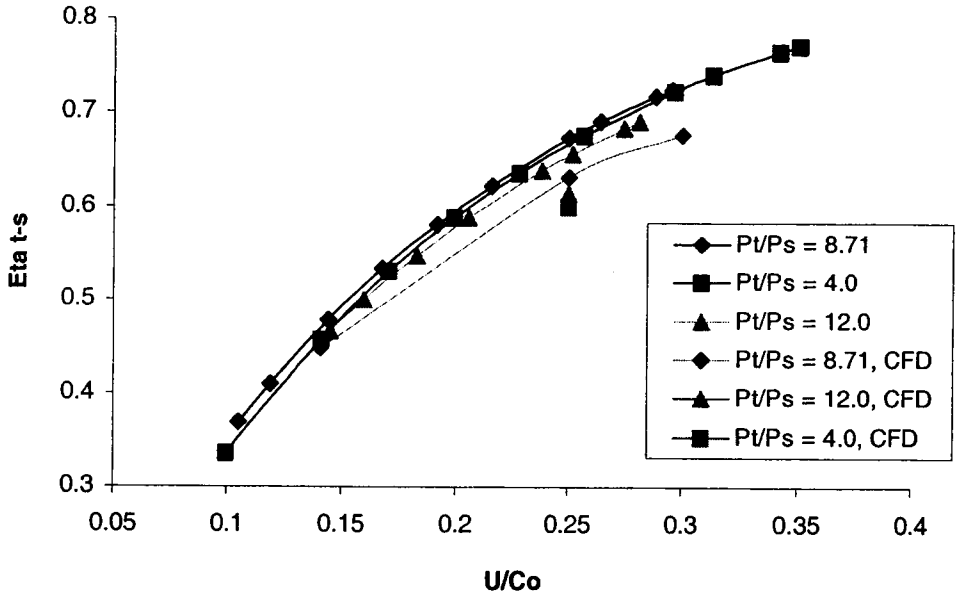

Figure 5. Efficiency vs. velocity ratio

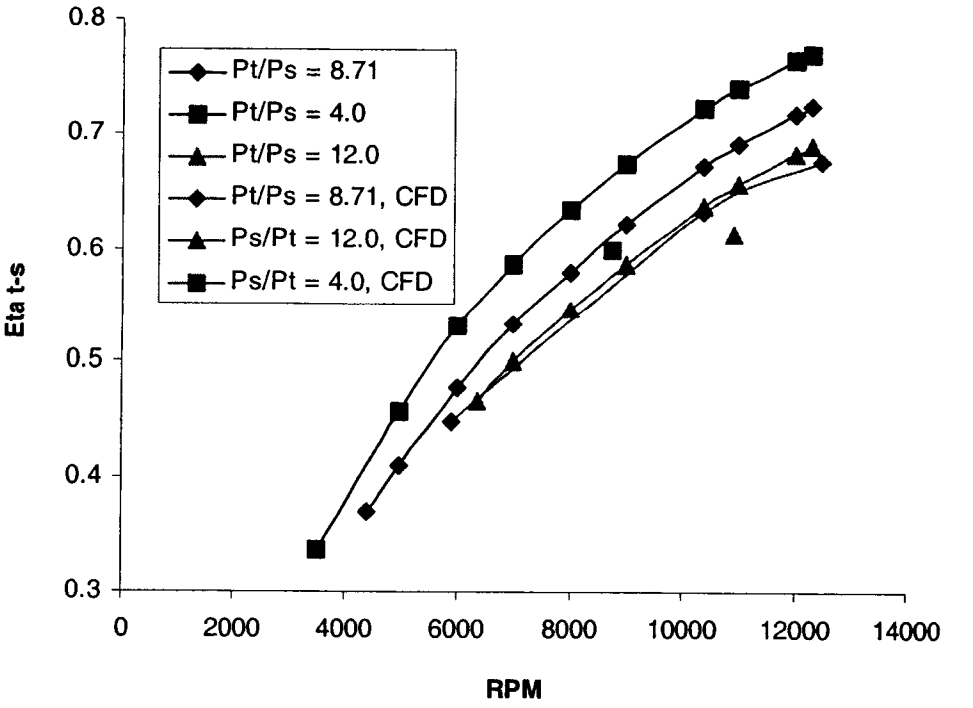

Figure 6. Efficiency vs. rotation speed

Figure 7. Instantaneous absolute Mach number - design

Figure 8. Instantaneous absolute Mach number - off-3

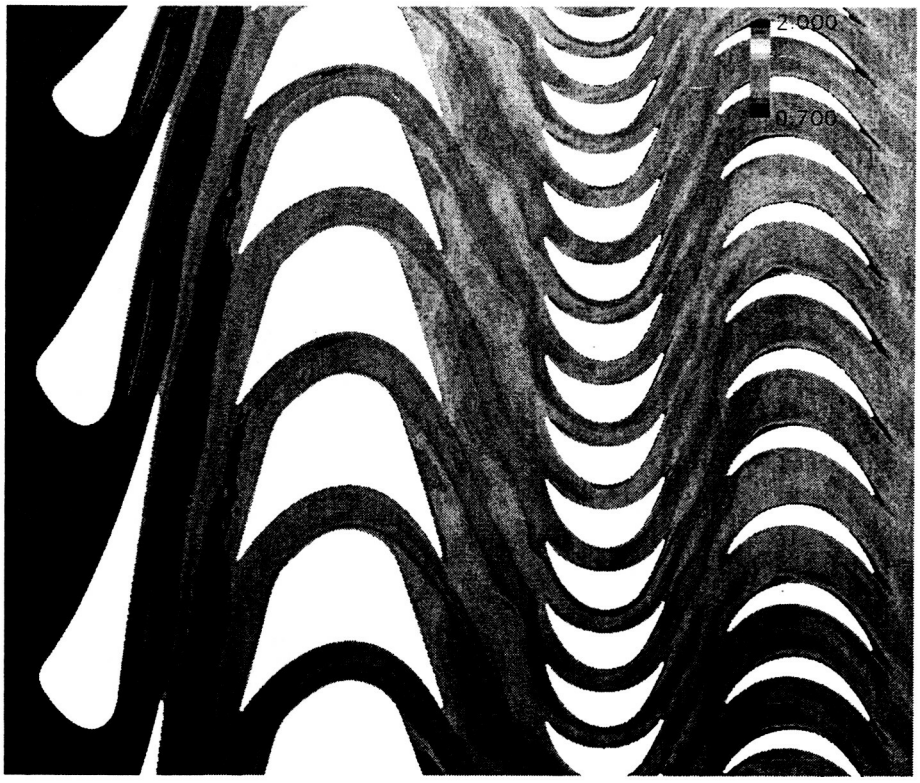

Figure 9. Instantaneous non-dimensional entropy - design

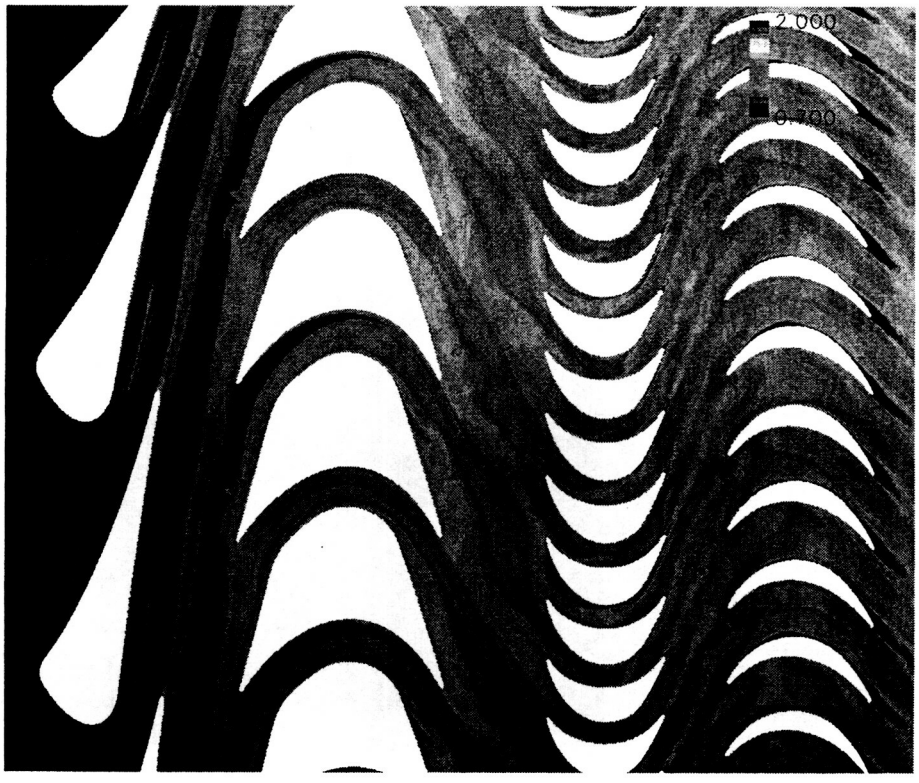

Figure 10. Instantaneous non-dimensional entropy - off-3

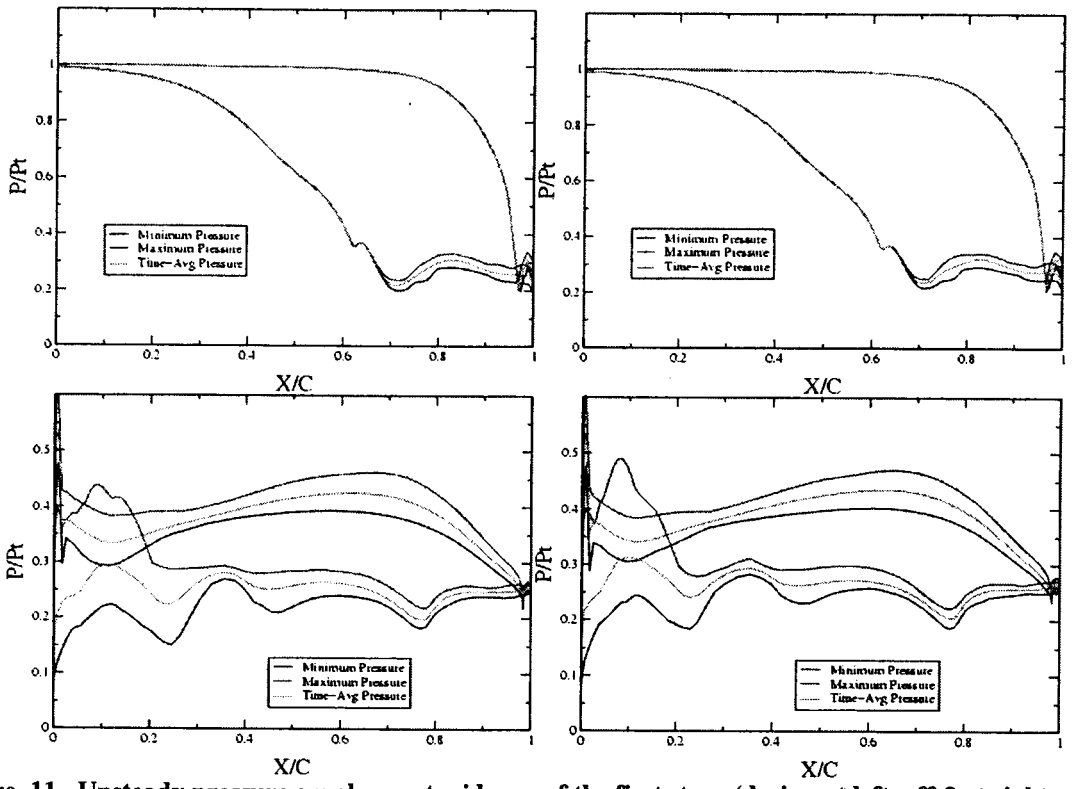

Figure. 11. Unsteady pressure envelopes at midspan of the first stage (design at left, off-3 at right, vanes top, rotors bottom)

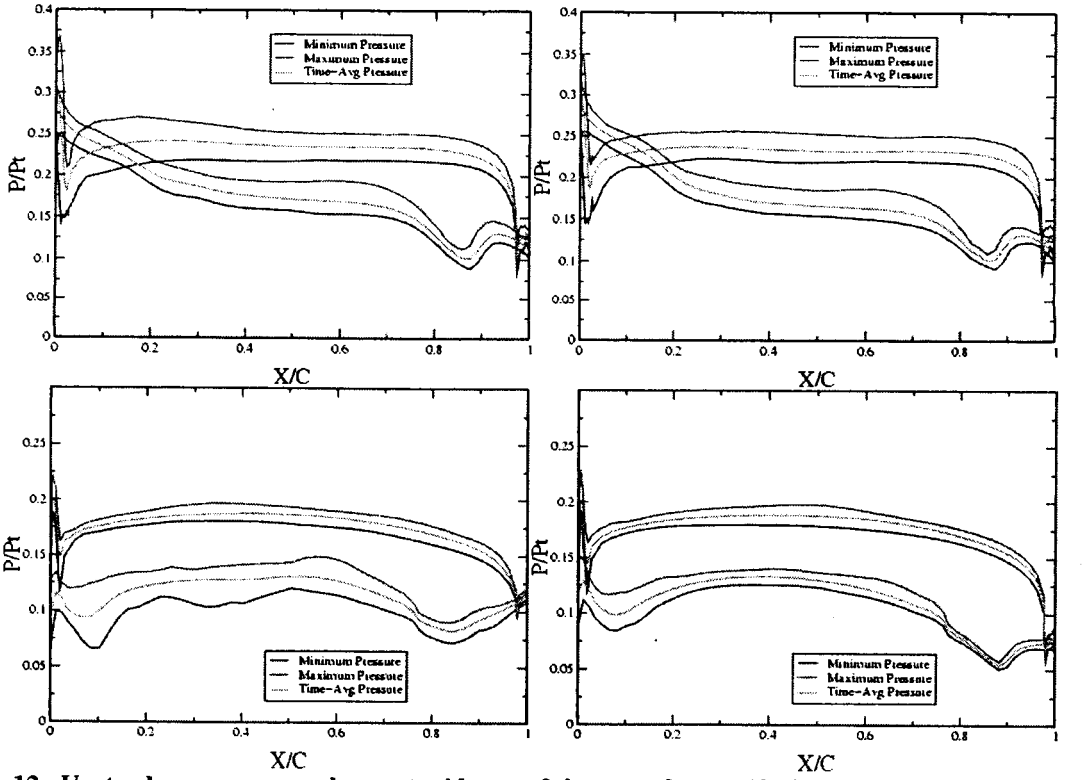

Figure. 12. Unsteady pressure envelopes at midspan of the second stage (design at left, off-3 at right, vanes top, rotors bottom)

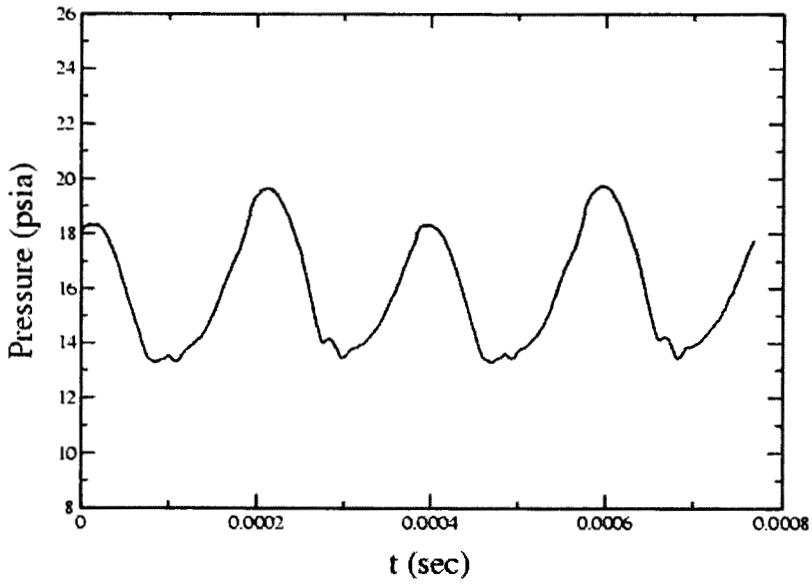

Figure 13. Unsteady pressure trace – midspan of first-stage vane trailing edge – design

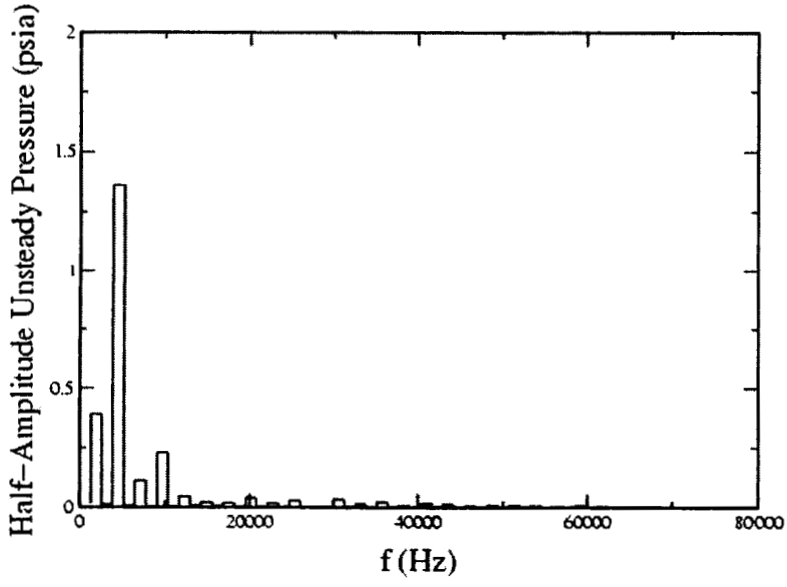

Figure 14. Fourier decomposition – midspan of first-stage vane trailing edge – design

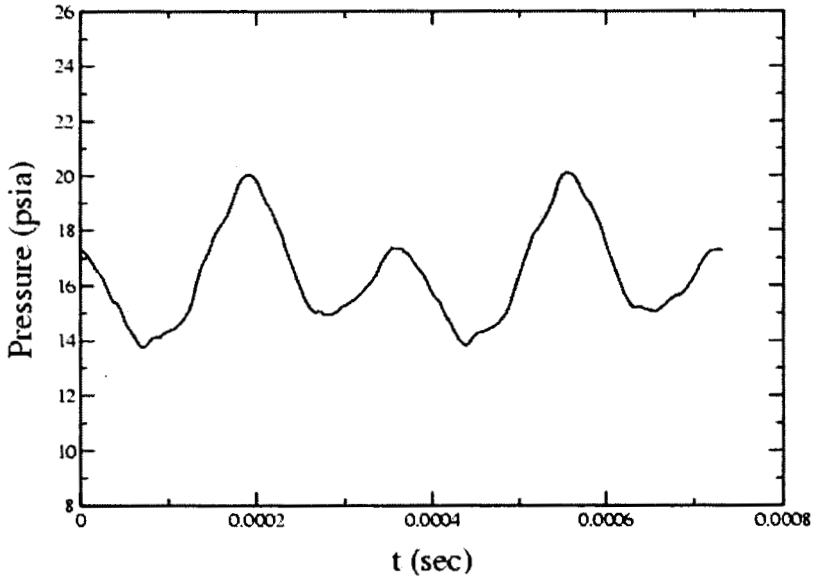

Figure 15. Unsteady pressure trace – midspan of first-stage vane trailing edge – off-3

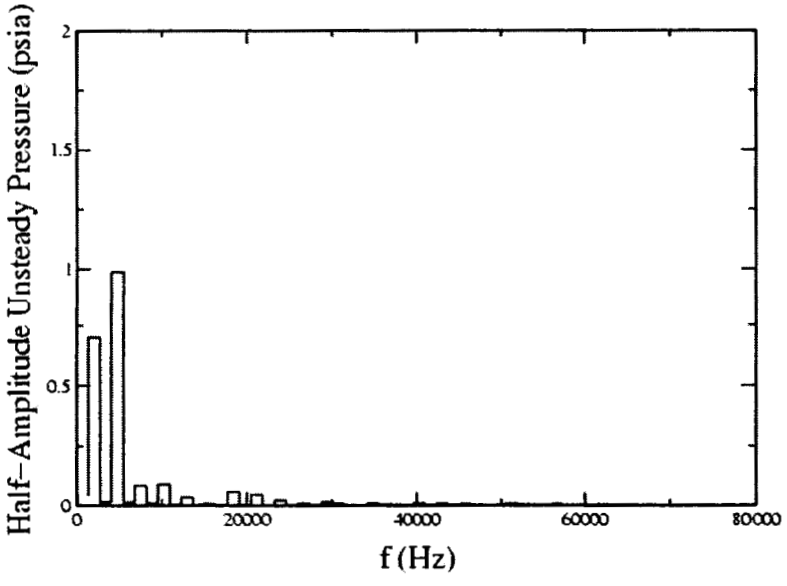

Figure 16. Fourier decomposition – midspan of first-stage vane trailing edge – off-3

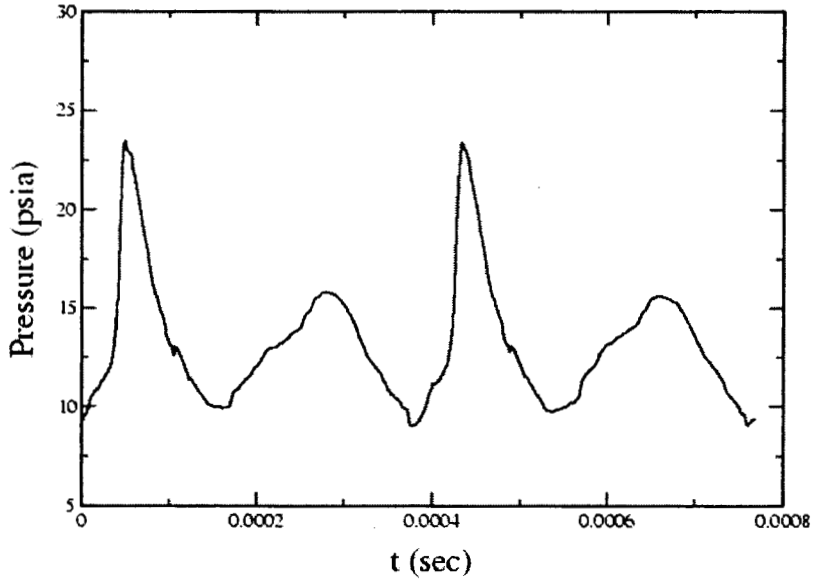

Figure 17. Unsteady pressure trace – midspan of first-stage rotor leading edge – design

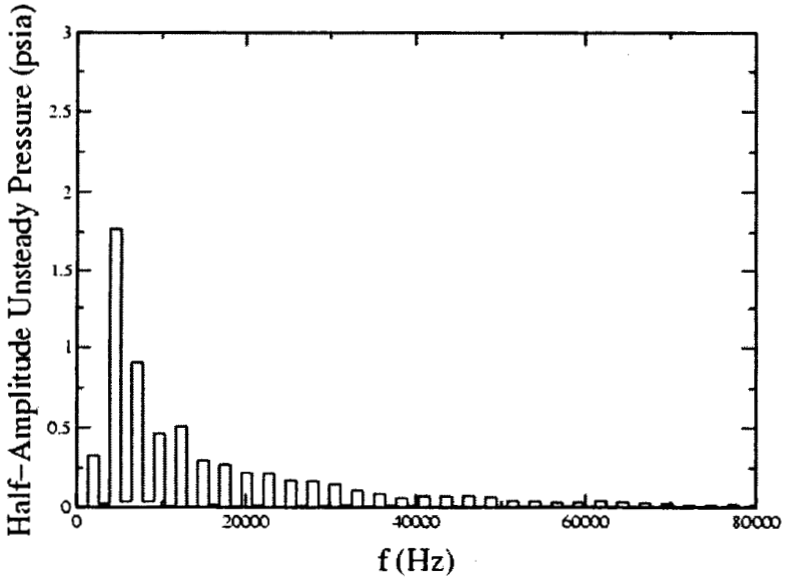

Figure 18. Fourier decomposition – midspan of first-stage rotor leading edge – design

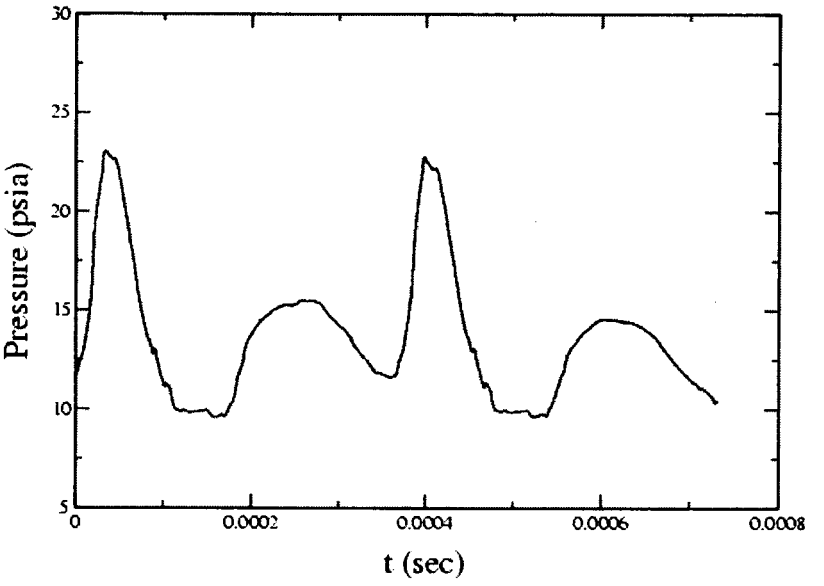

Figure 19. Unsteady pressure trace – midspan of first-stage rotor leading edge – off-3

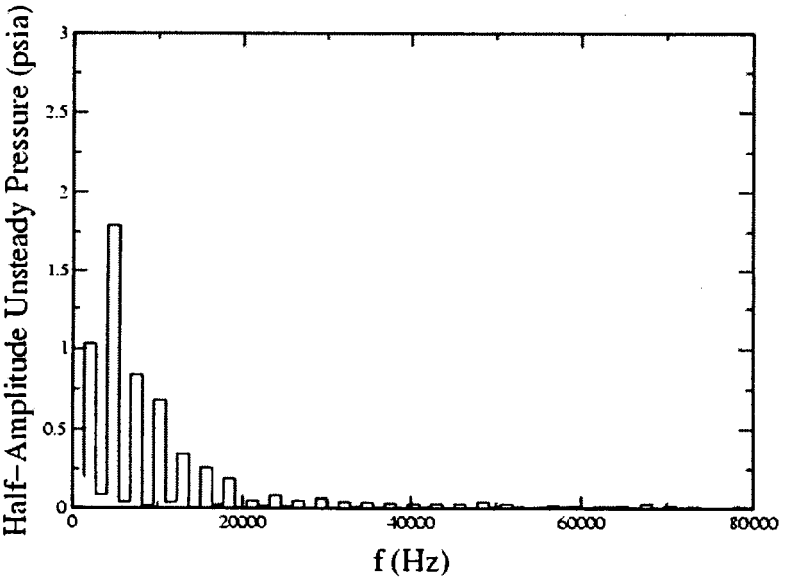

Figure 20. Fourier decomposition – midspan of first-stage rotor leading edge – off-3

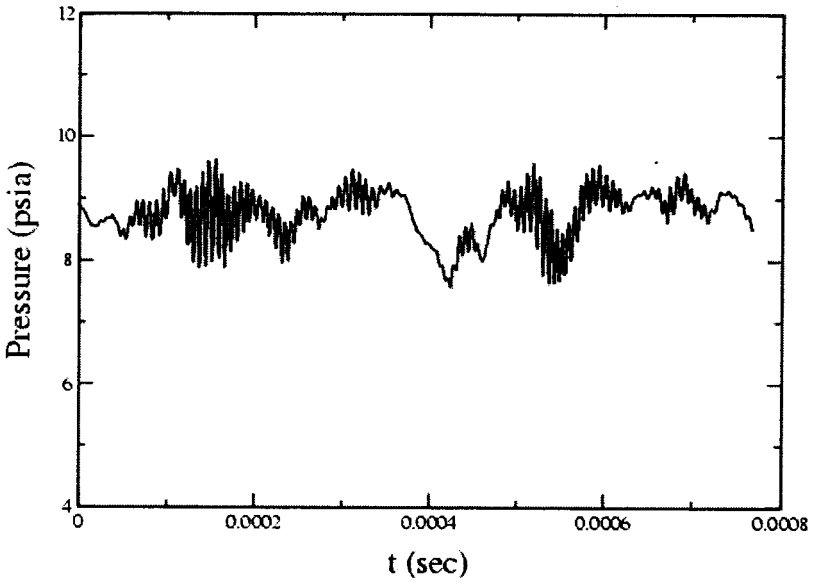

Figure 21. Unsteady pressure trace – midspan of second-stage vane trailing edge – design

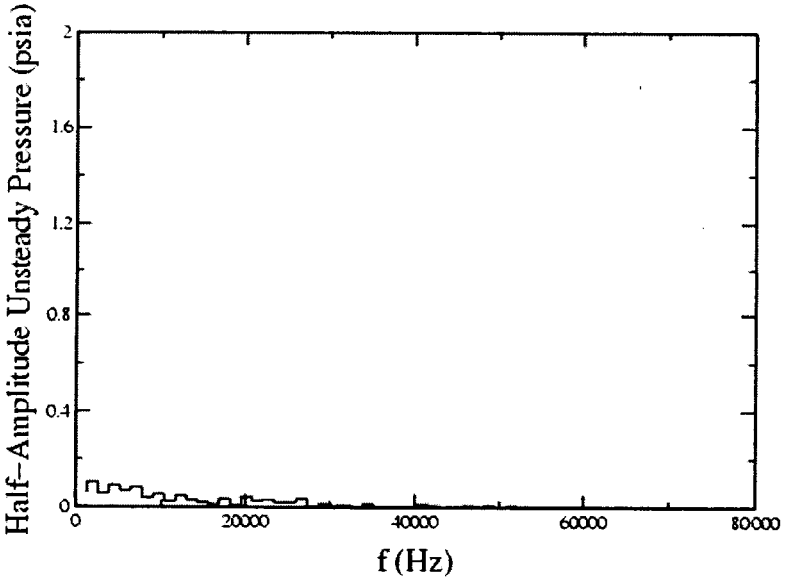

Figure 22. Fourier decomposition – midspan of second-stage vane trailing edge – design

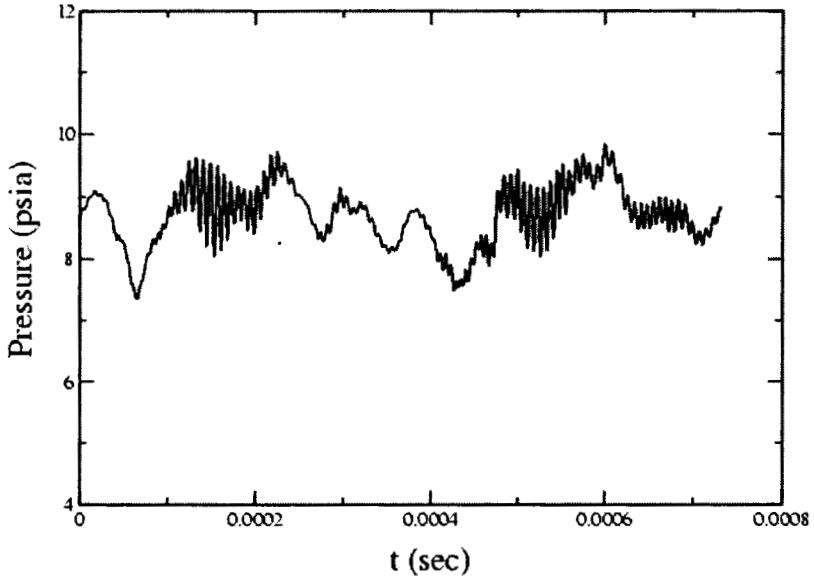

Figure 23. Unsteady pressure trace – midspan of second-stage vane trailing edge – off-3

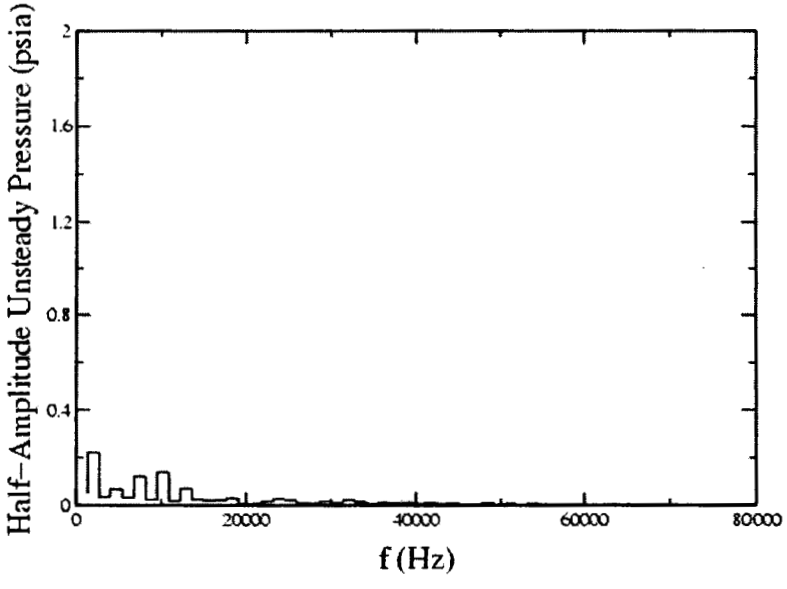

Figure 24. Fourier decomposition – midspan of second-stage vane trailing edge – off-3

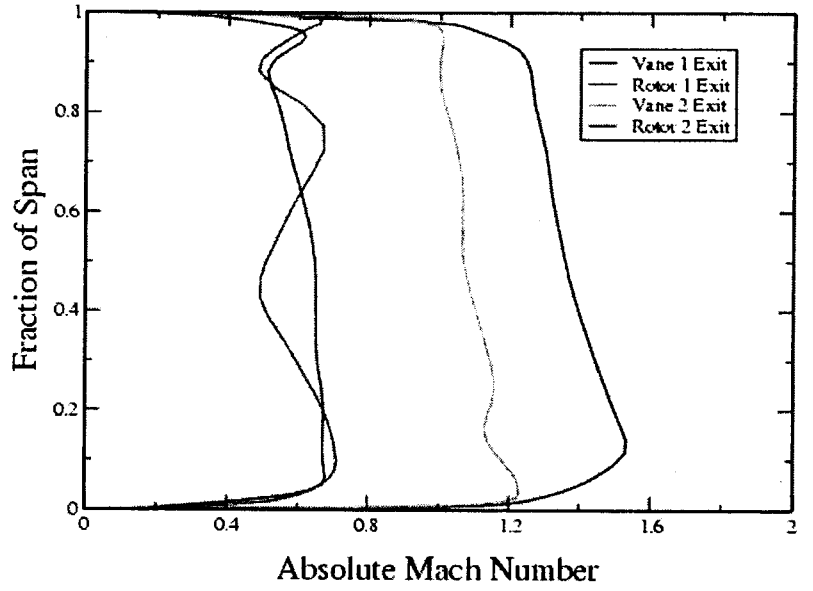

Figure 25. Radial profiles of circumferentially and time-averaged absolute Mach number – design.

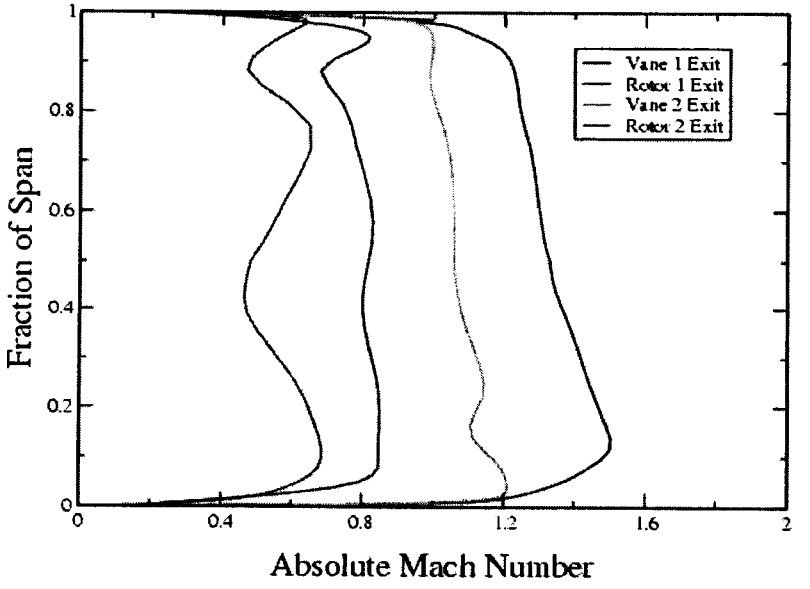

Figure 26. Radial profiles of circumferentially and time-averaged absolute Mach number – off-3

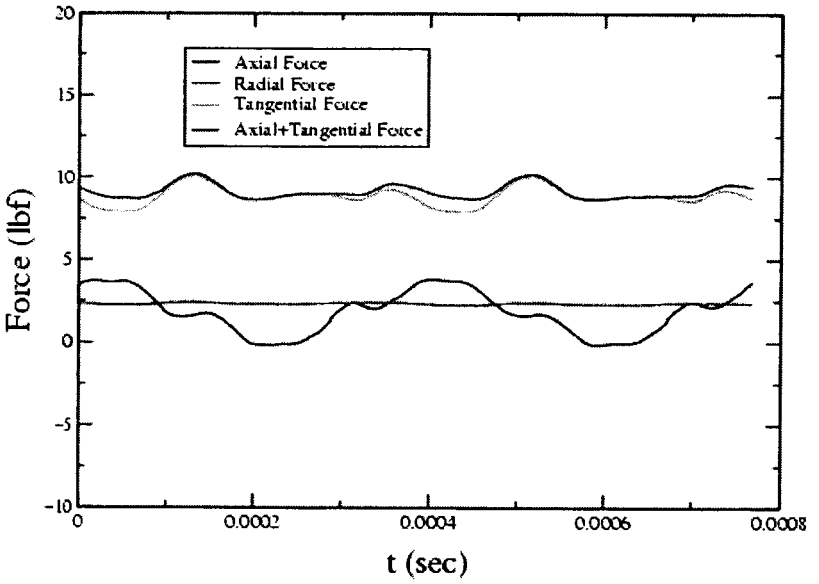

Figure 27. Unsteady integrated forces on the first-stage rotor – design

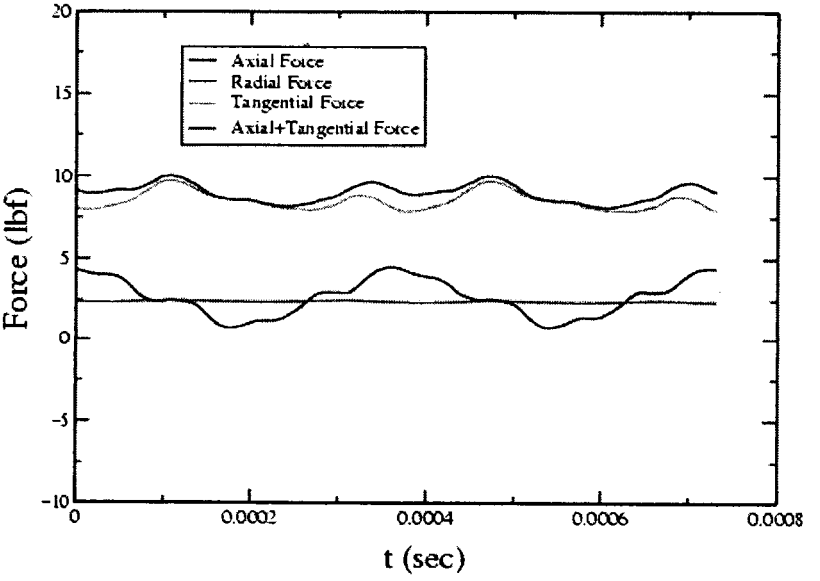

Figure 28. Unsteady integrated forces on the first-stage rotor – off-3

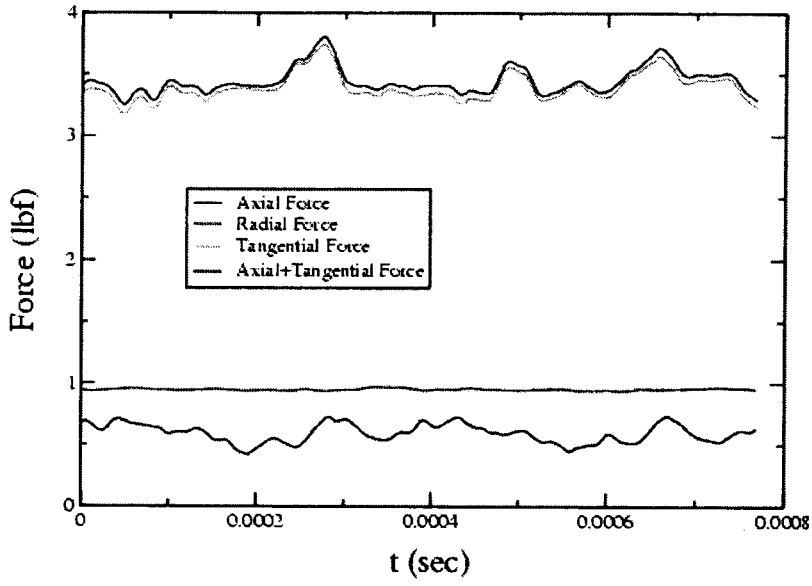

Figure 29. Unsteady integrated forces on the second-stage rotor – design

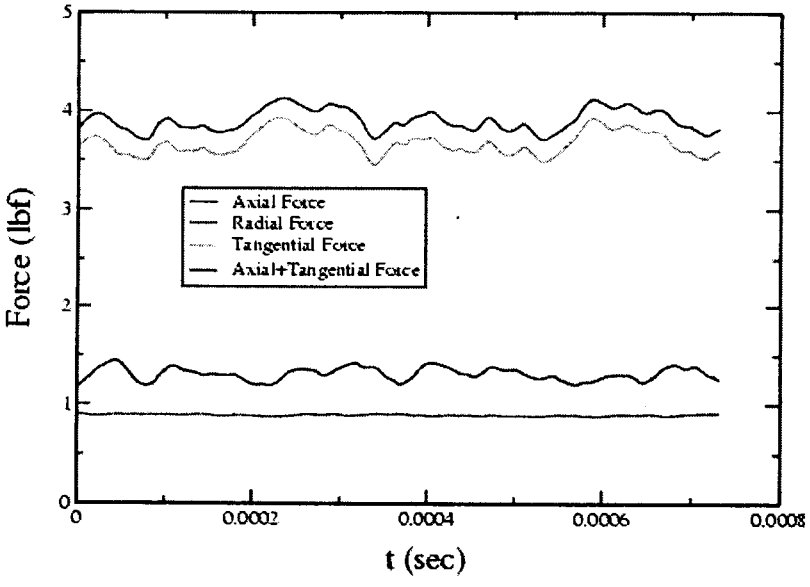

Figure 30. Unsteady integrated forces on the second-stage rotor – off-3